

# The influence of pore geometry and orientation on the strength and stiffness of porous rock



Luke Griffiths <sup>a,\*</sup>, Michael J. Heap <sup>a,\*\*</sup>, Tao Xu <sup>b</sup>, Chong-feng Chen <sup>b</sup>, Patrick Baud <sup>a</sup>

<sup>a</sup> Institut de Physique de Globe de Strasbourg, Université de Strasbourg/EOST, CNRS UMR 7516, France

<sup>b</sup> Center for Rock Instability and Seismicity Research, Northeastern University, Shenyang, 110819, China

## ARTICLE INFO

### Article history:

Received 10 December 2016

Received in revised form

3 February 2017

Accepted 10 February 2017

Available online 11 February 2017

### Keywords:

Aspect ratio

Pore angle

Porosity

Young's modulus

Uniaxial compressive strength

Numerical modelling

## ABSTRACT

The geometry of voids in porous rock falls between two end-members: very low aspect ratio (the ratio of the minor to the major axis) microcracks and perfectly spherical pores with an aspect ratio of unity. Although the effect of these end-member geometries on the mechanical behaviour of porous rock has received considerable attention, our understanding of the influence of voids with an intermediate aspect ratio is much less robust. Here we perform two-dimensional numerical simulations (Rock Failure Process Analysis, RFPA<sub>2D</sub>) to better understand the influence of pore aspect ratio (from 0.2 to 1.0) and the angle between the pore major axis and the applied stress (from 0 to 90°) on the mechanical behaviour of porous rock under uniaxial compression. Our numerical simulations show that, for a fixed aspect ratio (0.5) the uniaxial compressive strength and Young's modulus of porous rock can be reduced by a factor of ~2.4 and ~1.3, respectively, as the angle between the major axis of the elliptical pores and the applied stress is rotated from 0 to 90°. The influence of pore aspect ratio on strength and Young's modulus depends on the pore angle. At low angles (~0–10°) an increase in aspect ratio reduces the strength and Young's modulus. At higher angles (~40–90°), however, strength and Young's modulus increase as aspect ratio is increased. At intermediate angles (~20–30°), strength and Young's modulus first increase and then decrease as pore aspect ratio approaches unity. These simulations also highlight that the influence of pore angle on compressive strength and Young's modulus decreases as the pore aspect ratio approaches unity. We find that the analytical solution for the stress concentration around a single elliptical pore, and its contribution to elasticity, are in excellent qualitative agreement with our numerical simulations. The results of our numerical modelling are also in agreement with recent experimental data for porous basalt, but fail to capture the strength anisotropy observed in experiments on sandstone. We conclude that the alignment of grains or platy minerals such as clays exerts a greater influence on strength anisotropy in porous sandstones than pore geometry. Finally, we show that the strength anisotropy that arises as a result of preferentially aligned elliptical pores is of a similar magnitude to that generated by bedding in porous sandstones and foliation in low-porosity metamorphic rocks. The modelling presented herein shows that porous rocks containing elliptical pores can display a strength and stiffness anisotropy, with implications for the preservation and destruction of porosity and permeability, as well as the distribution of stress and strain within the Earth's crust.

© 2017 Elsevier Ltd. All rights reserved.

## 1. Introduction

Most rocks contain porosity in the form of pores, microcracks, or a combination of the two. Porosity is known to exert a first-order

control on the physical properties of rocks. For example, with increasing porosity, strength (e.g., Al-Harthy et al., 1999; Chang et al., 2006; Zhu et al., 2011; Baud et al., 2014; Schaefer et al., 2015) and Young's modulus (e.g., Chang et al., 2006) decrease and permeability increases (e.g., Bourbié and Zinszner, 1985; Farquharson et al., 2015; Wadsworth et al., 2016). These studies have shown that porosity alone (i.e. the scalar quantity) does not control the mechanical and hydraulic behaviour of rocks, highlighting an important role for the geometry of the void space (e.g.,

\* Corresponding author.

\*\* Corresponding author.

E-mail addresses: [luke.griffiths@unistra.fr](mailto:luke.griffiths@unistra.fr) (L. Griffiths), [heap@unistra.fr](mailto:heap@unistra.fr) (M.J. Heap).

Chang et al., 2006; Farquharson et al., 2015). The aspect ratio (the ratio of the minor to major semi axis) of an elliptical void within a rock will fall between two end-members: microcracks that have a very low aspect ratio ( $10^{-3} - 10^{-5}$ , Simmons and Richter, 1976) and perfectly spherical pores with an aspect ratio of unity. Indeed, recent advances in X-ray micro-computed tomography ( $\mu$ CT) have shown that porous rocks can contain a wide variety of pore shapes (e.g., Ji et al., 2012; Rozenbaum and Rolland du Roscat, 2014; Ji et al., 2015; Schmitt et al., 2016; Luquot et al., 2016; Arzilli et al., 2016; Bubeck et al., 2017; Zambrano et al., 2017).

Although two-dimensional micromechanical and numerical models exist to help understand the influence of uniformly aligned microcracks (e.g., Ashby and Sammis, 1990) and circular pores (e.g., Sammis and Ashby, 1986; Heap et al., 2014) on the mechanical behaviour of porous materials, including rocks, much less is known as to the influence of voids with an intermediate aspect ratio. A recent experimental study has shown, using uniaxial compressive strength tests, that basalt samples containing elliptical pores (aspect ratio  $\approx 0.5$ ) oriented with their major axis perpendicular to the loading direction were measurably weaker than those prepared to contain pores with their major axis parallel to loading (Bubeck et al., 2017). Although this study offers insight into the influence of non-spherical pores on mechanical behaviour, it remains challenging to isolate the influence of a specific parameter (e.g., pore aspect ratio, pore orientation with regards to the loading direction, and porosity) using natural samples, a consequence of their inherent variability. To circumvent natural variability, we use here a numerical modelling approach to isolate the role of select pore geometrical parameters (pore aspect ratio and pore orientation) on the compressive strength and Young's modulus of porous materials. We report on the results of numerical simulations, using the two-dimensional Rock Failure Process Analysis code (RFPA<sub>2D</sub>; Tang, 1997), in which we uniaxially deform rectangular samples populated with elliptical pores. Samples were built to contain different porosities (from 0.02 to 0.2), pore aspect ratios (from 0.2 to 1.0), and angles between the pore major axis and the loading direction (from 0 to 90°). Finally, the results of the RFPA<sub>2D</sub> modelling are compared with two-dimensional analytical solutions for the stress concentration around a single elliptical pore (from Jaeger et al., 2009) the contribution of the elliptical pore to the Young's modulus (from Kachanov et al., 1994). We also compare our modelled results with new and previously published experimental data (basalt, sandstone, and limestone), and compare the strength anisotropy generated by the preferential alignment of elliptical pores, bedding in porous sandstones, and foliation in low-porosity metamorphic rocks.

## 2. Description of numerical simulations

The two-dimensional Rock Failure Process Analysis code (RFPA<sub>2D</sub>) is a numerical model based on elastic damage mechanics (Tang, 1997). We used the model to uniaxially deform 400 × 200 pixel rectangular bitmap images that contained elliptical pores with a major axis of 20 pixels in length (Fig. 1). Considering a resolution of 0.1 mm/pixel, the images are analogous to rectangular samples 40 mm in length and 20 mm in width containing elliptical pores with a major axis of 2 mm. These samples were generated using a MATLAB script. To generate a bitmap image, we first selected a fixed pore aspect ratio (the ratio of the minor to major semi axis) and a fixed pore angle,  $\beta$ , (the angle measured from the vertical long axis of the rectangle and the major axis of the elliptical pore in a clockwise manner). We then iteratively added pores to the image in random locations until the target porosity was met. Pores were not allowed to overlap, although they could intersect the boundary of the image (Fig. 1). Each 0.1 mm square element was

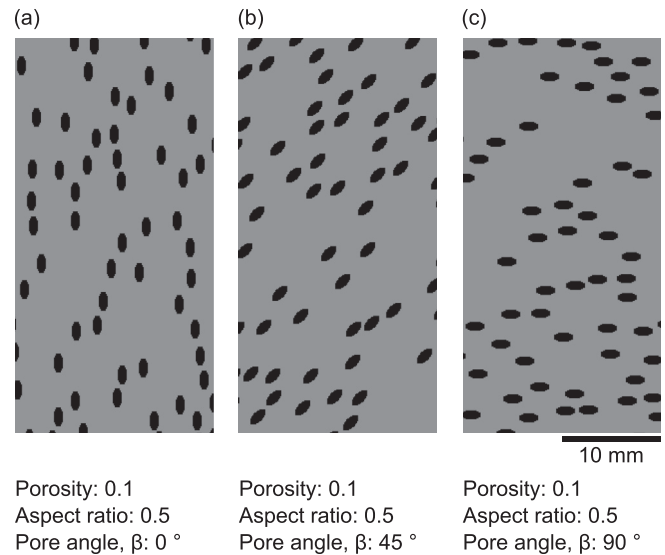


**Fig. 1.** Examples of randomly generated numerical samples containing a porosity of 0.1: elliptical pores with an aspect ratio of 0.5. Samples are rectangular bitmap images (400 × 200 pixels; 40 × 20 mm) containing elliptical pores with a major axis of 20 pixels in length (i.e. 2 mm). The angles between the vertical long axis of the rectangular sample (i.e. the loading direction) and the major axis of the elliptical pore,  $\beta$ , are (a) 0°, (b) 45°, and (c) 90°.

assigned a Young's modulus ( $E$ ) and a value of compressive ( $\sigma_{cr}$ ) and tensile ( $\sigma_{tr}$ ) strength. The pores were considered to have zero strength and Young's modulus, whilst the elements comprising the matrix were assigned values of strength and Young's modulus using a Weibull probability density function (Weibull, 1951; Wong et al., 2006):

$$x(u) = \frac{m}{u_0} \left(\frac{u}{u_0}\right)^{m-1} \exp\left[-\left(\frac{u}{u_0}\right)^m\right] \quad (1)$$

where  $x(u)$  is  $\sigma_{cr}(u)$ ,  $\sigma_{tr}(u)$ , or  $E(u)$ , and  $u$  and  $u_0$  are respectively the scale parameter of an individual element and the scale parameter of the average element (given in Table 1), respectively. We chose a matrix homogeneity factor  $m$ —the Weibull shape parameter—of 3 for all of our simulations. High values of  $m$  will yield more homogeneous samples (the property of a particular element will be closer to the chosen mean), and vice-versa (see Xu et al., 2012). Examples of the distribution (given by Equation (1)) of Young's modulus ( $E$ ) and uniaxial compressive strength ( $\sigma_{cr}$ ) are provided in Fig. 2 (for a sample containing 80,000 elements,  $m = 3$ , and the matrix element properties given in Table 1). Our matrix element properties (Table 1) and homogeneity factor ( $m = 3$ ) are the same as those used in the recent publications of Heap et al. (2014; 2015a; 2016). Although, for example, the mean uniaxial compressive

**Table 1**

The mean physical and mechanical properties of the matrix elements (i.e. the 0.1 mm squares that form the sample) used in the Rock Failure Process Analysis code (RFPA<sub>2D</sub>) numerical modelling. The value assigned to each element was determined using the Weibull probability function (Equation (1); see Fig. 2). The matrix element properties are the same as those used in the recent publications of Heap et al. (2014; 2015a; 2016).

Homogeneity index	3
Mean uniaxial compressive strength (MPa)	2300
Mean Young's modulus (GPa)	100
Poisson's ratio	0.25
Ratio of compressive to tensile strength	10
Frictional angle (°)	30

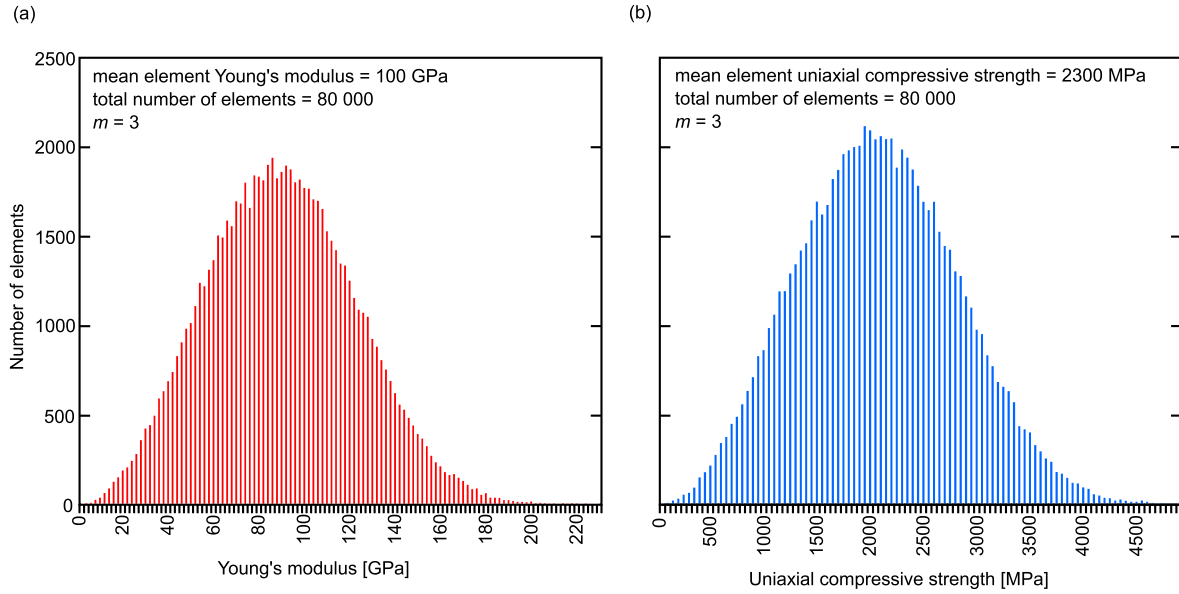


**Fig. 2.** Examples of the distribution of (a) Young's modulus and (b) uniaxial compressive strength for a sample with the mean element physical and mechanical properties given in Table 1 and a Weibull shape factor  $m = 3$  (the homogeneity factor). The sample contains 80,000 elements.

strength on the microscale appears high (Table 1), the homogeneity factor ensures that the elements within the sample contain a wide range of values (Fig. 2 shows that element compressive strength varies from ~100 to ~4500 MPa), similar to the microscale heterogeneities expected within a natural sample. Due to these microscale heterogeneities, the macroscopic strength is much less than the mean strength of an element on the microscale. Indeed, a sample containing zero porosity, using the mean microscale values in Table 1 and  $m = 3$ , has a uniaxial compressive strength of 553 MPa (Heap et al., 2014), a value similar to that of porosity-free borosilicate glass (Vasseur et al., 2013).

The rectangular samples were deformed uniaxially ( $\sigma_1 > \sigma_2 = \sigma_3 = 0$ ) in compression in 0.002 mm increments parallel to their vertical long axes. Following the first displacement increment, the axial stress,  $\sigma$ , acting on each 0.1 mm element was calculated using a linear elastic damage constitutive law:

$$\sigma = E_0(1 - D)\varepsilon \quad (2)$$

where  $D$  is the isotropic damage variable and  $\varepsilon$  is the axial strain. An element was considered damaged if one of two strength criteria were met, the maximum tensile strain criterion:

$$D = \begin{cases} 0 & \varepsilon_{t0} < \varepsilon \leq 0 \\ 1 - \frac{\sigma_{tr}}{\varepsilon E_0} & \varepsilon_{tu} < \varepsilon \leq \varepsilon_{t0} \\ 1 & \varepsilon \leq \varepsilon_{tu} \end{cases} \quad (3)$$

and the Mohr-Coulomb criterion:

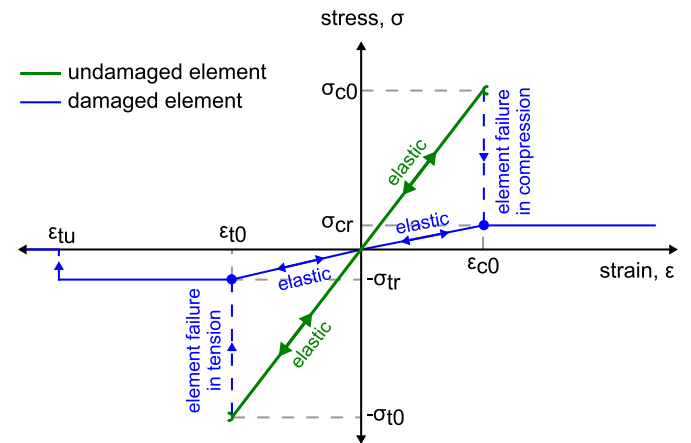
$$D = \begin{cases} 0 & 0 \leq \varepsilon < \varepsilon_{c0} \\ 1 - \frac{\sigma_{cr}}{\varepsilon E_0} & \varepsilon_{c0} \leq \varepsilon \end{cases} \quad (4)$$

Fig. 3 shows the axial stress as a function of axial strain for an individual element, calculated from Equation (2), using values of  $D$  from Equations (3) and (4). The ultimate tensile (extensional) strain of the element is given as  $\varepsilon_{tu}$  (Fig. 3). Further,  $\sigma_{tr} = \lambda\sigma_{t0}$ , where  $\lambda$  is the residual strength coefficient, and  $\sigma_{t0}$  is the uniaxial tensile strength at the elastic strain limit  $\varepsilon_{t0}$  (Fig. 3). The residual uniaxial

compressive strength  $\sigma_{cr}$  is defined as  $\sigma_{cr} = \lambda\sigma_{c0}$ , where  $\lambda$  is the residual strength coefficient, and  $\sigma_{c0}$  is the uniaxial compressive strength at the elastic strain limit  $\varepsilon_{c0}$  (Fig. 3). If an element was damaged, its Young's modulus was modified according to the elastic damage constitutive law (Lemaitre and Chaboche, 1994):

$$E = E_0(1 - D) \quad (5)$$

where  $E_0$  is the Young's modulus of the intact element. A Young's modulus of  $1.0 \times 10^{-5}$  GPa was assigned to any element for which  $D = 1$  to prevent the system of equations from being ill-posed. If no elements were damaged following the displacement increment (i.e. Equations (3) and (4) were not satisfied), the sample was subjected to the next 0.002 mm displacement increment. If a number of



**Fig. 3.** A schematic axial stress-strain curve for an element under uniaxial compressive and tensile stress, as calculated from the elastic damage constitutive law (Equation (2)). The green lines represent the axial stress-strain curves of the undamaged element in the elastic regime, in both compression and tension. The element may become damaged if it is deformed to a critical strain in tension ( $\varepsilon_{t0}$ ) or compression ( $\varepsilon_{c0}$ ) (see Equations (3) and (4)). The dashed blue lines show element failure in both compression and tension. The solid blue lines represent the axial stress-strain curves of a damaged element, in both compression and tension. (For interpretation of the references to colour in this figure, the reader is referred to the web version of this article.)

elements were damaged, the stress acting on each element within the sample was recalculated using Equation (2). This process continued until only very few elements were damaged during the calculation step, at which point the sample was subjected to the next 0.002 mm displacement increment. The simulation was halted once the sample had succumbed to macroscopic failure (the formation of a through going fracture). During the simulations, the elements within the modelled sample are fixed in the vertical direction, but can move freely in the horizontal direction (as is the case for uniaxial compressive strength experiments in the laboratory). A flow chart detailing the modelling procedure is given as Fig. 4.

### 3. Results

#### 3.1. Pore angle as a control on mechanical behaviour

To investigate the influence of the angle between the pore major axis and the applied stress,  $\beta$ , on the compressive strength and Young's modulus, we performed 24 simulations in which we varied the pore angle ( $\beta = 0\text{--}90^\circ$ ) but kept the porosity (0.1) and pore aspect ratio (0.5) constant (Fig. 5). We performed at least two simulations for each sample configuration, the results of which differ slightly due to the random placement of pores within the

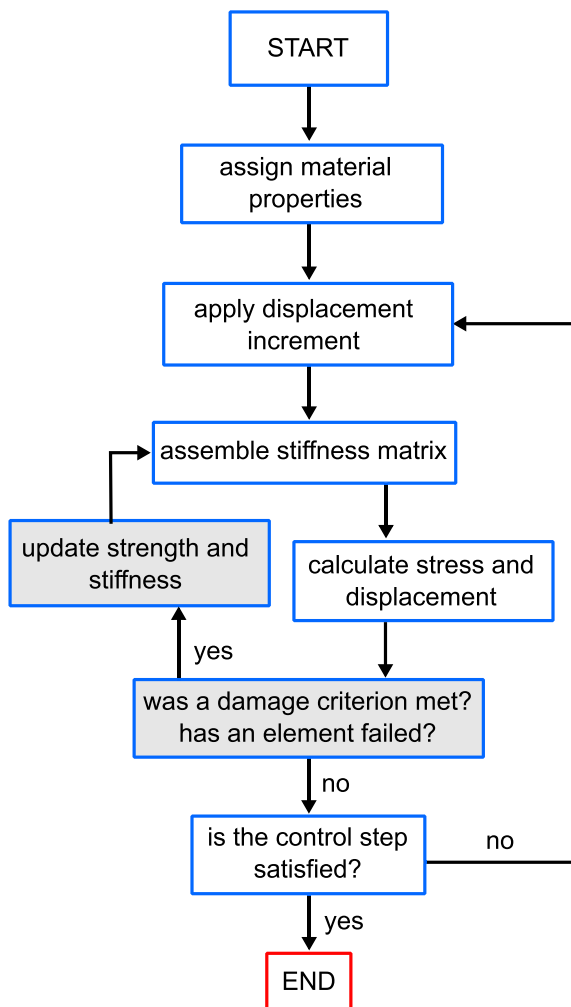


Fig. 4. A flow chart outlining the procedure for the Rock Failure Process Analysis (RFPA<sub>2D</sub>) code numerical model.

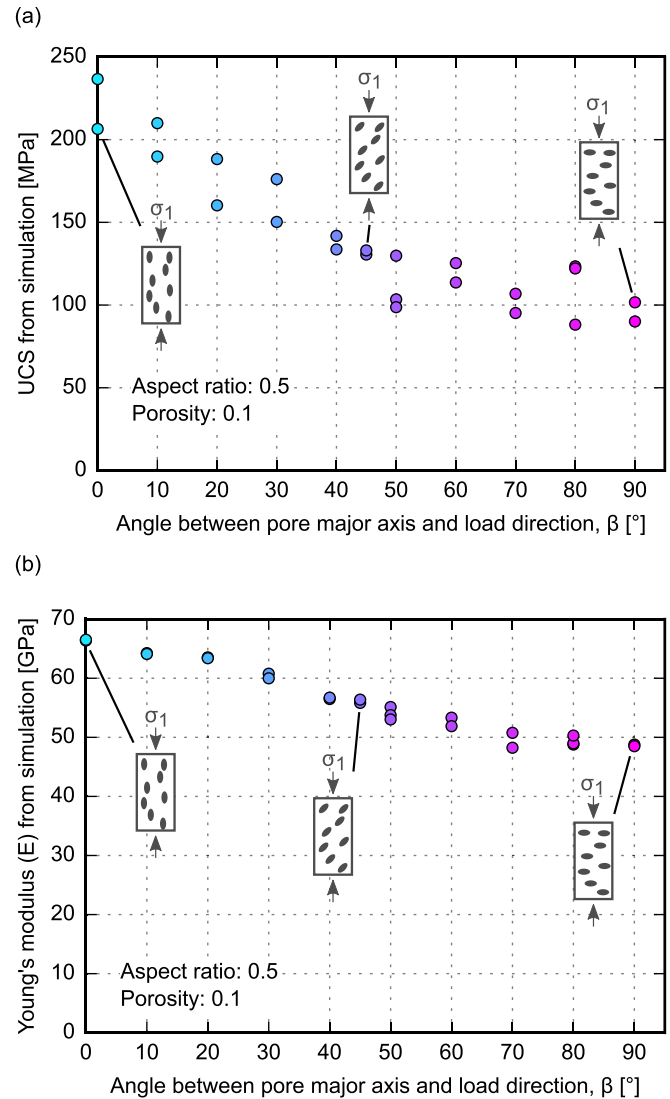
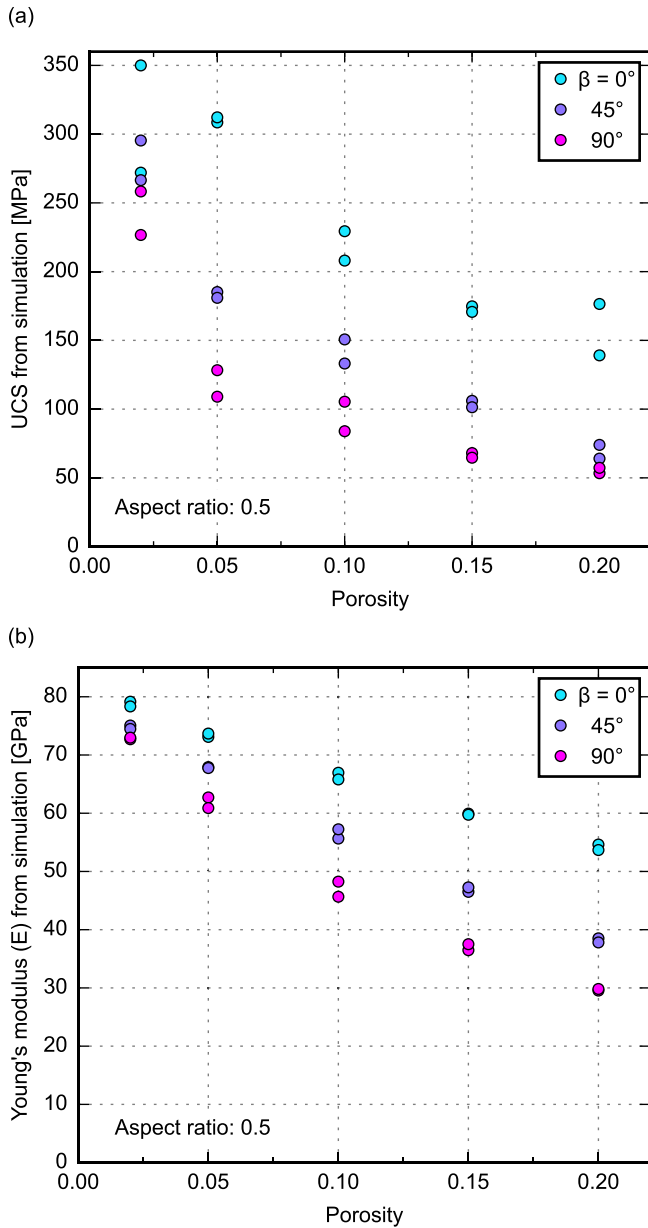


Fig. 5. The results of the Rock Failure Process Analysis (RFPA<sub>2D</sub>) code numerical modelling for (a) UCS and (b) Young's modulus as a function of the angle between the vertical long axis of the rectangular sample (i.e. the loading direction) and the major axis of the elliptical pore,  $\beta$ . The 2D numerical samples have a porosity of 0.1 and contain pores 2 mm in length with an aspect ratio of 0.5. The symbol colour (shades from turquoise to pink) refers to the angle between the major pore axis and the loading direction; this colour scheme is used here for consistency and ease of comparison between the figures of this manuscript. (For interpretation of the references to colour in this figure, the reader is referred to the web version of this article.)

generated sample (using our MATLAB script) and the fact that the elements are assigned their physical properties based on the Weibull probability density function shown in Equation (1). The simulations show that the uniaxial compressive strength and Young's modulus decrease from ~225 to ~100 MPa and from ~67 to ~50 GPa, respectively, as the angle between the pore major axis and the loading direction,  $\beta$ , increases from 0 to  $90^\circ$  (Fig. 5).

To understand the influence of pore angle on the mechanical behaviour of samples containing different porosities, we performed an additional 24 simulations in which we varied the porosity (from 0.02 to 0.2) and pore angle ( $\beta = 0, 45, \text{ and } 90^\circ$ ) for a fixed pore aspect ratio of 0.5 (Fig. 6). We performed at least two simulations for each sample configuration. The relative reduction in strength as the pore angle is increased from 0 to  $90^\circ$  remains essentially constant at porosities between 0.02 and 0.2 (Fig. 6a). However, our



**Fig. 6.** The results of the Rock Failure Process Analysis (RFP2D) code numerical modelling for (a) UCS and (b) Young's modulus as a function of porosity for samples containing elliptical pores of 2 mm length and 0.5 aspect ratio, with major axes at angles of 0, 45, and 90° to the vertical long axis of the rectangular sample (i.e. the loading direction).

simulations show that the relative reduction in Young's modulus with increasing pore angle is greater when the porosity is higher (Fig. 6b). For example, Young's modulus is only reduced from ~80 to ~74 GPa as pore angle,  $\beta$ , is increased from 0 to 90° at a porosity of 0.02, but is reduced from ~54 to 30 GPa at a porosity of 0.2 (Fig. 6b).

### 3.2. Pore aspect ratio as a control on mechanical behaviour

To investigate the influence of the pore aspect ratio on compressive strength and Young's modulus, we performed over a hundred numerical simulations in which we varied the aspect ratio (from 0.2 to 1.0) and pore angle ( $\beta = 0-90^\circ$ ), but kept the porosity fixed at 0.1 (Fig. 7). We performed at least two simulations for each sample configuration. Our simulations show that the influence of

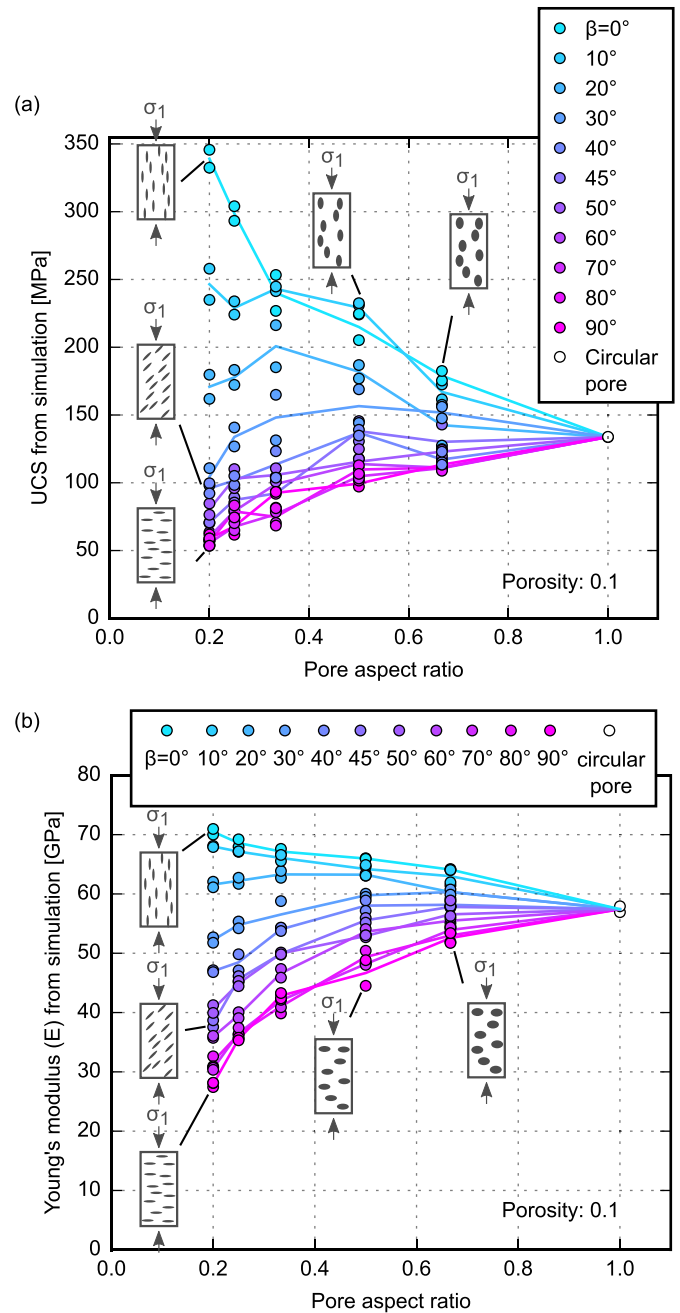


**Fig. 7.** The results of the Rock Failure Process Analysis (RFP2D) code numerical modelling for (a) UCS and (b) Young's modulus as a function of pore aspect ratio for samples containing a porosity of 0.1 and elliptical pores of 2 mm length with their major axes at angles of 0, 10, 20, 30, 40, 45, 50, 60, 70, 80, and 90° to the vertical long axis of the rectangular sample (i.e. the loading direction),  $\beta$ . Lines on the graphs connect the mean value of UCS and Young's modulus for each pore angle.

pore aspect ratio (from 0.2 to 1.0) on strength and Young's modulus depends on the pore angle. For low angles ( $\beta = 0-10^\circ$ ) an increase in aspect ratio results in reductions to strength and Young's modulus (Fig. 7). For higher angles ( $\beta = 40-90^\circ$ ) between the pore major axis and the loading direction, strength and Young's modulus increase with increasing aspect ratio (Fig. 7). At intermediate angles ( $\beta = 20-30^\circ$ ), strength and Young's modulus first increase and then decrease as pore aspect ratio is increased (Fig. 7). Pore aspect ratio also controls the magnitude of the difference in compressive strength and Young's modulus as pore angle,  $\beta$ , increases. For

example, strength decreases from ~225 to ~100 MPa (a decrease of about a factor of two) as the angle,  $\beta$ , increases from 0 to 90° for an aspect ratio of 0.5 (the results shown in Fig. 5). However, for an aspect ratio of 0.2, strength decreases from ~350 to ~50 MPa (a decrease by a factor of seven) for the same increase in angle,  $\beta$  (Fig. 7). The influence of pore angle,  $\beta$ , on compressive strength and Young's modulus decreases as the pore aspect ratio approaches unity (Fig. 7).

## 4. Discussion

### 4.1. Comparison with analytical solutions for stress and strain around a single elliptical pore

Our numerical simulations show that the geometry and orientation of elliptical pores influences the strength and Young's modulus at the sample lengthscale (Figs. 5–7). In the following section, we aim to provide a qualitative explanation for these results using existing analytical solutions for the stress concentration around a single elliptical pore, and its contribution to elasticity. Since these solutions are for a single pore, they do not account for pore interaction. Pore interaction may become non-negligible when pores are separated by less than the length of a pore major axis (Rice, 1997; Tsukrov and Kachanov, 1997), which is likely the case for some of our high-porosity numerical samples.

#### 4.1.1. Analytical solution for the stress along the pore boundary

The analytical solution for the tangential, or hoop stress, along the boundary of a two-dimensional elliptical void in an infinite medium, under an applied (“far-field”) uniaxial stress  $\sigma_1$ , is given by Equation (6) (Jaeger et al., 2009). The hoop stress is a function of  $\sigma_1$ , the lengths of the major and minor semi-axes of the ellipse, here  $a$  and  $b$  respectively, the angle of the major axis with regards to the loading direction,  $\beta$ , and the location along the ellipsis boundary given by the angle,  $\eta$ , in elliptical coordinates:

$$\tau_{\eta\eta} = \sigma_1 \frac{2ab - (a^2 - b^2)\cos(2\beta) - (a + b)^2\cos(2(\beta - \eta))}{a^2 + b^2 - (a^2 - b^2)\cos(2\eta)} \quad (6)$$

For a given applied stress ( $\sigma_1$ ), pore aspect ratio, and angle between the pore major axis and the loading direction ( $\beta$ ), the hoop stress has a maximum along the pore boundary, which we note  $\tau_{\eta\eta_{\max}}$ . Fig. 8a shows the applied stress,  $\sigma_1$ , required to generate a hoop stress of 1 MPa as the angle between the major axis and the loading direction,  $\beta$ , is increased from 0 to 90°. The applied stress required to generate a maximum hoop stress of 1 MPa is higher when the pore angle,  $\beta$ , is lower (Fig. 8a). Therefore, pores oriented so that their major axes are perpendicular to the direction of a given applied stress will intensify the stress to a greater extent than pores oriented parallel to that stress. This is in accord with the results from our numerical simulations: the strongest samples contain pores with their major axes oriented parallel to the loading direction, and the weakest samples contain pores oriented perpendicular to loading (Fig. 5a).

Fig. 8b shows the values of applied stress,  $\sigma_1$ , required for a maximum hoop stress  $\tau_{\eta\eta_{\max}}$  of 1 MPa for a single pore of varying aspect ratio (0.2–1) and angle to the loading direction ( $\beta = 0$ –90°). For the end-member scenario of circular pores (aspect ratio of unity), the applied stress required to maintain the hoop stress at 1 MPa is constant with pore angle,  $\beta$ , because the geometry is invariant by rotation. However, we observe a complex relationship between the applied stress and hoop stress with pore angle,  $\beta$ , and aspect ratio for an elliptical pore. At low pore angles (i.e. pores parallel or sub-parallel to the applied stress;  $\beta = 0$ –10°), an increase

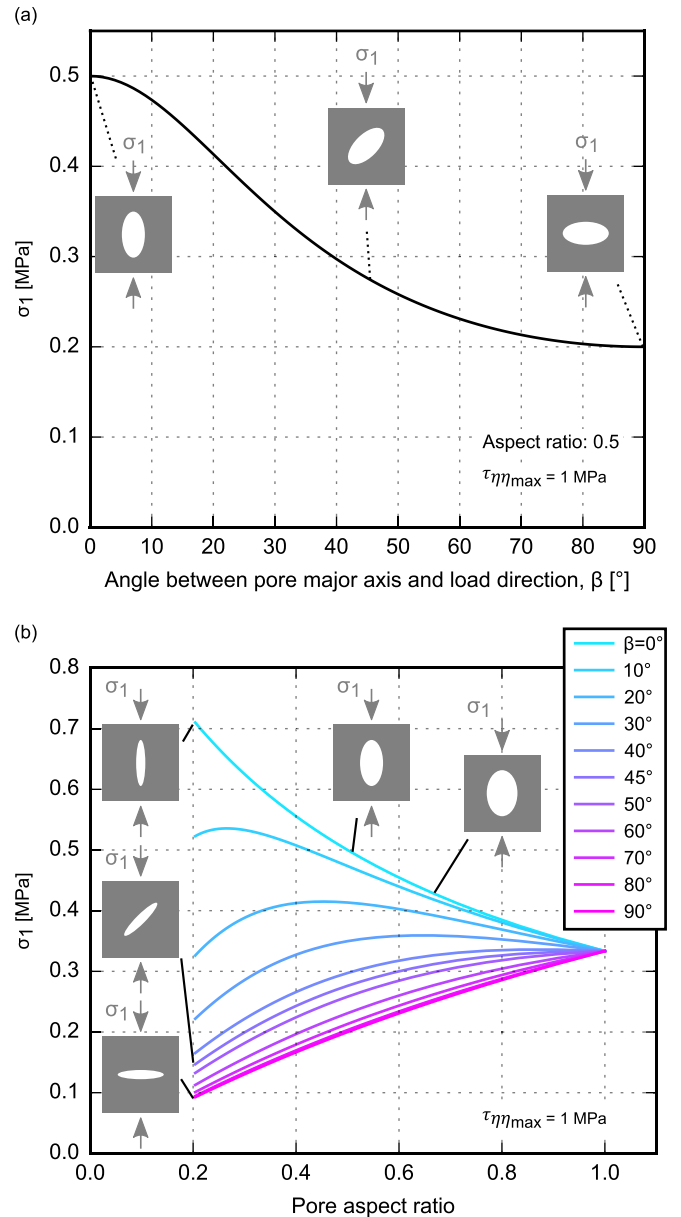


**Fig. 8.** (a) The applied (“far-field”) stress required for a maximum hoop stress of 1 MPa along the boundary of a 2D elliptical pore of aspect ratio 0.5, as a function of the angle between the major axis of the elliptical pore and the uniaxial loading direction ( $\beta = 0$ –90°) (calculated using Equation (6)). (b) The applied (“far-field”) stress required for a maximum hoop stress of 1 MPa along the boundary of a 2D elliptical pore as a function of aspect ratio (ranging from 0.2 to 1), for angles of 0, 10, 20, 30, 40, 45, 50, 60, 70, 80, and 90° between the pore major axis and the uniaxial loading direction,  $\beta$  (calculated using Equation (6)).

in pore aspect ratio decreases the value of the applied stress needed to maintain the hoop stress. However, at greater pore angles (pores perpendicular or sub-perpendicular to the applied stress;  $\beta = 40$ –90°) an increase in aspect ratio increases the applied stress required to maintain the hoop stress (Fig. 8b). At intermediate angles ( $\beta = 20$ –30°), the applied stress required to maintain the hoop stress first increases and then decreases as pore aspect ratio increases (Fig. 8b). We also note that the influence of pore angle,  $\beta$ , on strength decreases as the pore aspect ratio approaches unity (Fig. 8b).

The evolution of the stress intensification with pore angle and aspect ratio (Fig. 8) is in excellent qualitative agreement with the

evolution of strength in the numerical samples (Figs. 5a and 7a). The analytical solutions (Fig. 8) therefore suggest that the magnitude of the stress calculated on the boundary of a single elliptical pore is directly related to the macroscopic strength of a sample containing multiple pores of equivalent geometry (Figs. 5a and 7a).

#### 4.1.2. Analytical solution for pore elasticity

The Young's modulus of a two-dimensional elliptical void, oriented so that its major axis is parallel ( $\beta = 0^\circ$ ) (Equation (7)) or perpendicular ( $\beta = 90^\circ$ ) (Equation (8)) to the applied ("far-field") stress can be calculated from its strain response under uniaxial loading (Kachanov et al., 1994). The Young's modulus of the pore oriented with its major axis parallel and perpendicular to the loading direction is a function of  $a$  and  $b$ , the lengths of the major and minor semi-axes of the pore, and  $E_0$ , the Young's modulus of the rock matrix:

$$E_{\parallel} = E_0 \frac{a}{a + 2b} \quad (7)$$

$$E_{\perp} = E_0 \frac{b}{2a + b} \quad (8)$$

Fig. 9 shows the ratio of the pore and the rock matrix Young's moduli against pore aspect ratio (ranging from 0.2 to 1), for pores oriented with their major axes at 0 and 90° to the direction of the applied stress. For a given  $E_0$ , the Young's modulus of the pore oriented with its major axis parallel to the applied stress ( $\beta = 0^\circ$ ) decreases with increasing pore aspect ratio (Fig. 9). By contrast, the Young's modulus of the pore in the perpendicular direction ( $\beta = 90^\circ$ ) increases with increasing pore aspect ratio (Fig. 9). The same trend is observed in our numerical simulations (Fig. 7b).

Furthermore, Kachanov et al. (1994) show that in the presence of multiple pores, even when randomly oriented, the porosity alone is not enough to determine the bulk elastic properties; the pore aspect ratio is required. This is reflected in the results of our two-dimensional numerical simulations, where variations in pore aspect ratio (Fig. 7b) may in certain cases have a greater influence on the Young's modulus than the porosity (Fig. 6b).

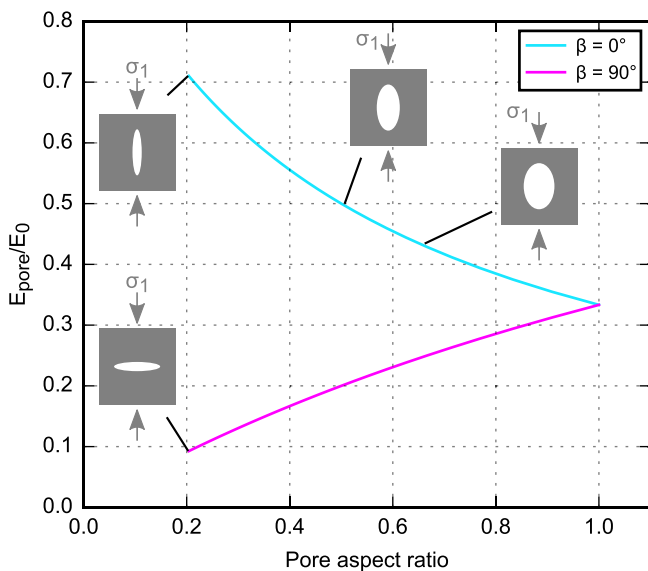


Fig. 9. The ratio of the Young's modulus of a 2D elliptical pore and the Young's modulus of the rock matrix as a function of pore aspect ratio (ranging from 0.2 to 1), for pores with their major axes oriented at 0 and 90° to the applied ("far-field") stress,  $\beta$  (calculated using Equations (7) and (8)).

## 4.2. Comparison with experimental data

### 4.2.1. Comparison with porous basalt data

We consider the numerical modelling presented herein to be particularly relevant for extrusive volcanic rocks (the pores are more likely to approximate an ellipse in extrusive volcanic rocks than in clastic materials, for which the pores are the interstitial voids between grains or fragments). The pores preserved in volcanic rocks are the frozen relicts of bubbles in magma, the shape and orientation of which can be modified by a number of volcanic processes (Shea et al., 2010). For example, magmas can experience significant strains during their ascent in the volcanic conduit, a process that can stretch and elongate bubbles (Arbaret et al., 2007; Okumura et al., 2010; Shields et al., 2014; Kushnir et al., 2017). In extreme cases, such shearing can form tube pumice, a rock that contains pores with a very low aspect ratio (Martí et al., 1999; Wright et al., 2006; Dingwell et al., 2016). Pore shape anisotropy preserved in volcanic rocks can also be the result of, for example, rheomorphic flow (Andrews and Branney, 2011) or viscous compaction (Quane et al., 2009; Heap et al., 2017).

We will now compare the strengths and Young's moduli from our numerical simulations with recently published experimental data on porous basalts (Bubeck et al., 2017). The mean pore aspect ratio for the basalts of Bubeck et al. (2017) was determined to be 0.32–0.54, and we plot these data together with our simulated output for a pore aspect ratio of 0.5 in Fig. 10. Although the absolute values of compressive strength and Young's modulus for the basalt are considerably lower than for our numerical samples (since the strengths and Young's moduli of our samples depends on the pre-selected element parameters in Table 1) we see that, similar to our simulations, the basalt is weaker when the applied stress is at 90° to the preferred orientation of the pore major axes than at 0° (Fig. 10). The anisotropy of the strength and Young's modulus can be expressed by the ratio of the mean value for an angle of 0° over the mean value for 90°. Anisotropy values for strength and Young's modulus for our numerical simulations and the experiments of Bubeck et al. (2017) are given in Table 2. The Young's modulus anisotropy factor for the basalt (average porosity = 0.165) experiments is 1.7 (Table 2). This value lies between those calculated for the simulated samples containing a porosity of 0.15 and 0.2: 1.6 and 1.8, respectively (Table 2). The strength anisotropy factor is however lower for the experimental data than for our simulations (Table 2). The experiments yield a strength anisotropy factor of 2.0, while the simulations containing porosities of 0.15 and 0.2 provide values of 2.6 and 2.9, respectively (Table 2). We interpret this discrepancy as a result of the pore geometry variability (radius, shape, orientation) in the natural samples. For example, the pore size is variable (the basal zone basalts contain pores with volumes  $\ll 5 \text{ mm}^3$  and  $> 5 \text{ mm}^3$ )—a factor that affects the stress intensification at the tip of a pore-emanating microcrack (Sammis and Ashby, 1986)—and the major axes of the pores will not all be parallel. By contrast, all the pores in the numerical simulations have an identical geometry and orientation. Nevertheless, we find that our numerical simulations are in good overall agreement with the porous basalt data of Bubeck et al. (2017).

### 4.2.2. Comparison with sandstone and limestone data

The pores of a clastic rock such as sandstone are the interstitial voids between grains and, as a result, an ellipse may not best represent their shape. Nevertheless, we consider it interesting to compare our modelled results with data for sandstone, since the pores within sandstone are commonly preferentially oriented with their major axis parallel to bedding (i.e. they are likely to exhibit a pore shape anisotropy). Indeed, anisotropy of magnetic susceptibility (AMS) has revealed a pore shape anisotropy in sandstones:

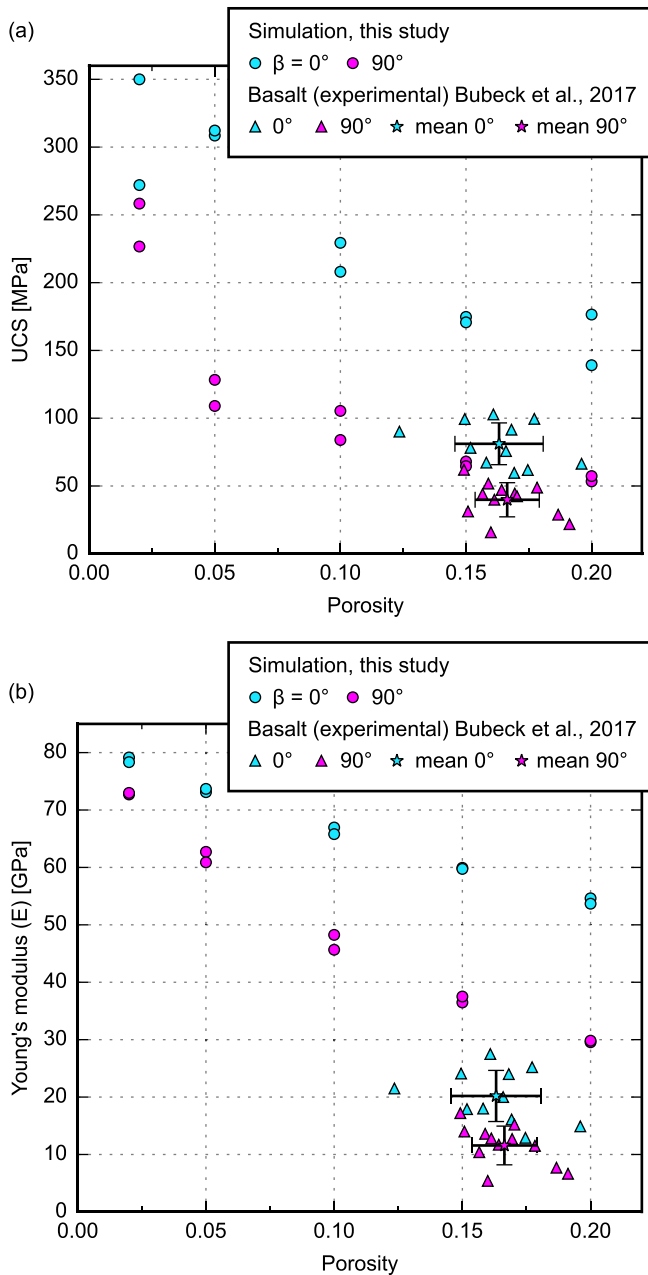


**Fig. 10.** (a) UCS and (b) Young's modulus as a function of porosity from our numerical simulations, plotted alongside data from a recent experimental study on basalt of Bubeck et al. (2017). The numerical samples contain pores with an aspect ratio of 0.5 that are oriented so that their major axis is at an angle of  $0$  or  $90^\circ$  to the vertical long axis of the rectangular sample (i.e. the loading direction),  $\beta$ . The basalt samples have a mean aspect ratio in the range of 0.32–0.54 (Bubeck et al., 2017). The experimental data shown here are for basalt samples prepared so that their pore major axis is orientated at an angle of  $0$  or  $90^\circ$  to the sample axis (i.e., the loading direction). For the Bubeck et al. (2017) data, we also plot the mean values for each pore orientation with the standard deviation.

the pore major axis in a wide variety of porous sandstones was found to be sub-parallel to bedding (Louis et al., 2003; Benson et al., 2005; Robion et al., 2014). Recent advances in  $\mu$ CT have also provided a detailed description of the shape of pores within sandstone. For example, Schmitt et al. (2016) showed that pore shapes in reservoir sandstones are typically plate- and cube-like.

Mechanical data from uniaxial and triaxial experiments on sandstone show that they are strongest when deformed

perpendicular to bedding (Baud et al., 2005 and references therein; Louis et al., 2009). For example, the peak stress of Rothbach sandstone deformed at an effective pressure of 5 MPa was  $\sim 60$  MPa when the sample was deformed perpendicular to bedding, and  $\sim 50$  MPa when the sample was deformed parallel to bedding (Louis et al., 2009). These porous sandstones are therefore weaker when the loading direction is parallel to the pore major axis, an observation in conflict with the modelling results (Fig. 5a) and the experimental data for porous basalt (Bubeck et al., 2017). We complement existing data on strength anisotropy in porous sandstones by performing constant strain rate ( $10^{-5} \text{ s}^{-1}$ ) uniaxial compressive strength (UCS) tests on dry sandstone cores (20 mm in diameter and nominally 40 mm in length) prepared so that their axes were either parallel or perpendicular to bedding (Table 3). The four sandstones chosen—Adamswiller (e.g., Baud et al., 2006), Rothbach (e.g., Louis et al., 2009), Bleurswiller (e.g., Heap et al., 2015b), and Bentheim (e.g., Klein et al., 2001)—contain similar connected porosities (0.225–0.245; Table 3) and have similar average grain diameters ( $\sim 200 \mu\text{m}$ ). The results of our uniaxial deformation experiments are in agreement with the data presented in Baud et al. (2005) and Louis et al. (2009): the sandstones are systematically weaker when they are deformed parallel to bedding (ratios of perpendicular to parallel strength are between 1.12 and 1.54; Table 3). Based on these and the published data, we conclude that pore shape anisotropy in sandstone may not play a first-order role in dictating their strength anisotropy. The alignment of grains or platy minerals such as clays may therefore control strength anisotropy in the porous sandstones studied here. Indeed, Louis et al. (2003, 2009) concluded that the mechanical anisotropy observed in Rothbach sandstone was the result of the preferential alignment of grains. A result of this preferential alignment is that the total grain-to-grain contact surface is highest when the sample is loaded perpendicular to bedding. In this scenario, the stress on the individual contacts is at its lowest and the macroscopic strength of the sample is high as a result. By contrast, the total grain-to-grain contact area is lowest when the sample is loaded parallel to bedding. In this scenario, the stress on the individual contacts is at its highest, allowing microcracks to form at a lower given applied stress, and the macroscopic strength of the sample is low as a result (Louis et al., 2003, 2009). We further note that, although the pore shapes within sandstones can be approximated as plate- or cube-like (Schmitt et al., 2016), they are typically much less defined than the pores found within extrusive volcanic rocks, especially basalts (Bubeck et al., 2017).

Several studies have observed a pore shape anisotropy in limestones (e.g., Ji et al., 2012, 2015; Robion et al., 2014; Zambrano et al., 2017). For example, Ji et al. (2012, 2015) showed that the sphericity of macropores within Indiana and Majella limestone (limestones that contain a dual porosity of micro- and macropores) decreases as their equivalent diameter increases. While the majority of micropores in Indiana limestone (pores with a diameter  $< 33 \mu\text{m}$ ) have a sphericity  $> 0.78$ , macropores with an equivalent diameter of  $> \sim 200 \mu\text{m}$  are characterised by a sphericity of  $\leq 0.59$  (Ji et al., 2012). Data for Majella limestone were similar: the majority of micropores are close to a sphericity of unity, while macropores  $> \sim 100 \mu\text{m}$  are characterised by a sphericity of  $\leq 0.59$  (Ji et al., 2015). A combination of AMS and P-wave velocity data for Jurassic limestones from the Western part of the Paris Basin revealed prolate pores with their major axis typically orientated parallel to bedding (Robion et al., 2014). However, comparison between our modelled results and data for carbonate rocks is difficult not only due to the paucity of laboratory strength anisotropy data, but also the lack of studies that combine pore geometry analysis and mechanical testing. UCS tests on microporous Oxfordian limestones from the Eastern part of the Paris Basin showed no

**Table 2**

Unconfined compressive strength (UCS) and Young's modulus (*E*) anisotropy factors for the numerical simulations (this study) and the experimental data for basalt from Bubeck et al. (2017). Anisotropy factors were calculated using the mean values of UCS and Young's modulus.

	Porosity	UCS anisotropy factor	<i>E</i> Anisotropy factor
Numerical, this study	0.02	1.3	1.1
	0.05	2.6	1.2
	0.1	2.3	1.4
	0.15	2.6	1.6
	0.2	2.9	1.8
Experimental (basalt), Bubeck et al. (2017)	0.165 (mean)	2.0	1.7

evidence of mechanical anisotropy (Baud et al., 2016), whilst limestones from Central Anatolia were found to be strongest when deformed perpendicular to bedding and weakest when the bedding was at an angle of 30° to the loading direction (Karakul et al., 2010). Studies on limestones combining detailed pore geometry and orientation analysis with mechanical strength testing are now required to test the modelled predictions presented herein (Figs. 5–7).

4.3. Strength anisotropy in crustal rocks

Strength anisotropy in crustal rocks is typically attributed to planar fabrics in rock, such as bedding in sedimentary rocks (e.g., Millien, 1993; Baud et al., 2005; Louis et al., 2003, 2009) or foliation in metamorphic rocks (e.g., Donath, 1972; Shea and Kronenberg, 1993; Baud et al., 2005). Here we have shown that significant strength anisotropy can also arise as a result of the preferential alignment of elliptical pores (Figs. 5–7; see also Bubeck et al., 2017). Interestingly, the evolution of strength as a function of the angle between the applied stress and each of these three fabrics—bedding, foliation, and pore major axis—is markedly different (Fig. 11). As this angle is increased from 0 to 90°, the strength of sandstone increases, the strength of basalt decreases, and the strength of phyllite first decreases (with a minimum at about 45°) and then increases (Fig. 11). Fig. 11 highlights that the strength anisotropy as a result of the preferential alignment of elliptical pores is of a similar magnitude to that for bedding and foliation. The numerous sources of mechanical anisotropy in the crust, and their varied contribution to such anisotropy (Fig. 11), highlight the importance of orienting rocks either collected or catalogued in the field and providing a complete description of their textural heterogeneity.

4.4. Implications

The results from our numerical simulations highlight that the aspect ratio of elliptical pores (the ratio of the minor to major axis) and the angle of their major axis with respect to the loading

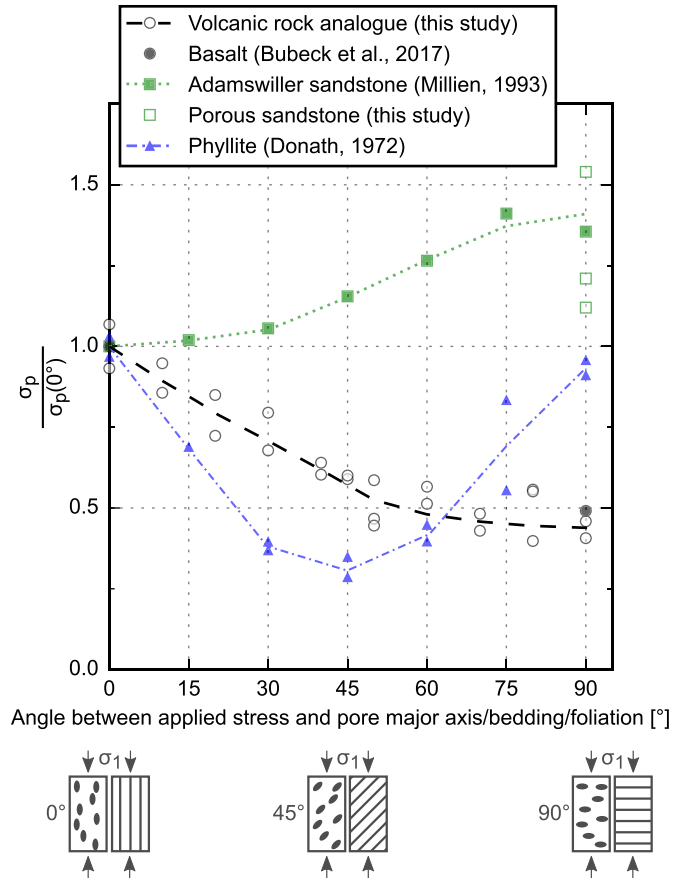


**Fig. 11.** The ratio between the peak stress ( $\sigma_p$ ) and the peak stress when the angle between the applied stress and the pore major axis/bedding/foliation is 0° ( $\sigma_{p(0^\circ)}$ ) as a function of the angle between the applied stress and the pore major axis/bedding/foliation. For the sandstone data (uniaxial compressive strength tests on Adamswiller sandstone, taken from Millien, 1993; and uniaxial compressive strength tests from this study, Table 3), the angle corresponds to the angle between the applied stress and the bedding. For the volcanic rock analogue (the simulations of this study; porosity = 0.1 and pore aspect ratio = 0.5) and basalt data (uniaxial compressive strength tests on basalt from Kilauea (Hawaii, USA), taken from Bubeck et al., 2017), the angle corresponds to the angle between the applied stress and the pore major axis. For the phyllite data (triaxial compressive strength tests on Moretown phyllite performed at a confining pressure of 50 MPa, taken from Donath, 1972), the angle corresponds to the angle between the applied stress and the foliation. We also provide cartoons to illustrate the direction of the applied stress ( $\sigma_1$ ) with regard to the pore major axis (cartoon on the left) and the bedding/foliation (cartoon on the right).

direction play important roles in controlling rock strength (Figs. 5a, 6a and 7a) and stiffness (Figs. 5b, 6b and 7b). Therefore, porous rock containing preferentially oriented elliptical pores can exhibit a considerable strength and stiffness anisotropy. Further, elliptical pores with their major axis oriented perpendicular to the direction

**Table 3**

Unconfined compressive strength (UCS) of sandstone samples deformed either parallel or perpendicular to bedding (data unique to this study).

Sample	Connected porosity	Orientation of sample axis with respect to bedding	Uniaxial compressive strength (MPa)	Ratio of perpendicular ( $\sigma_{p(90^\circ)}$ ) to parallel ( $\sigma_{p(0^\circ)}$ ) strength
Adamswiller	0.245	Perpendicular	49.4	1.21
Adamswiller	0.245	Parallel	40.8	
Rothbach	0.225	Perpendicular	26.7	1.54
Rothbach	0.225	Parallel	17.3	
Bleurswiler	0.240	Perpendicular	41.4	1.21
Bleurswiler	0.240	Parallel	34.3	
Bentheim	0.230	Perpendicular	47.8	1.12
Bentheim	0.230	Parallel	41.3	

of loading may control the strength of rock containing randomly oriented non-spherical pores. These results explain in part the variability that is typically observed in plots of UCS as a function of porosity for porous rock (e.g., Chang et al., 2006; Baud et al., 2014; Schaefer et al., 2015; Heap et al., 2016; Zhu et al., 2016; Bubeck et al., 2017).

In this study we considered the influence of pore geometry and orientation and porosity on the strength and stiffness of porous rock. We did not consider changes in pore size, a variable exposed to influence both strength and stiffness in two-dimensional micromechanical (Sammis and Ashby, 1986) and numerical (Heap et al., 2014) modelling of materials containing circular pores. Recent data on basalts from Mt. Etna (Italy) showed that porosity and pore size are not necessarily independent: higher porosity samples had larger pores, and vice-versa (Zhu et al., 2016). Future modelling efforts on the mechanical influence of pore geometry and orientation should therefore consider variations in pore size.

Through comparison of our modelling results with new and previously published experimental data, we can conclude that the modelling presented herein is particularly relevant for extrusive volcanic rocks, but does not capture the complexity of sandstones, for which grain orientation may play an important role in dictating their strength anisotropy (e.g., Louis et al., 2009). Discrete element methods (DEM), in which grains can be represented as circular disks or spheres, may better capture the behaviour of clastic materials such as sandstones (e.g., Wang et al., 2008). There are unfortunately too few data to make firm conclusions as to whether our modelled results are relevant for porous limestones.

As demonstrated by our modelling, and the experimental data of Bubeck et al. (2017), the preserved pore shape and orientation in volcanic rock can greatly impact their strength and stiffness (Figs. 5–7). Therefore, if the pore major axis is typically oriented parallel to bedding in lavas, as was the case for the basalts collected from the south flank of Kīlauea, Hawaii (Bubeck et al., 2017), then the rocks will be weaker and less stiff in the vertical direction, and stronger and stiffer in the horizontal direction. These rocks may therefore be more prone to porosity and permeability reduction driven by vertical lithostatic stresses than similarly porous rock with spherical pores. By contrast, and as discussed in Bubeck et al. (2017), such rocks may be better equipped to withstand horizontal stresses (such as tectonic stresses, or stresses transferred from the magma-filled conduit to the adjacent volcanic rock during volcanic unrest) that could help to safeguard against reductions to porosity and permeability at depths where the rocks will compact in response to an applied stress (Heap et al., 2015c, 2017), or prevent faulting at shallow depths. A pronounced strength anisotropy could therefore create permeability heterogeneity within a reservoir or volcanic edifice.

Large differences in the strength and Young's modulus of superimposed layers of volcanic rock, such as the difference between a stiff and strong lava layer and a compliant and weak tuff layer, can promote dyke arrest and therefore impede dyke-fed eruptions (Gudmundsson, 2006), and influence fault zone architecture and fluid flow (Walker et al., 2013). Our modelling has demonstrated that differences in pore shape and orientation between superimposed layers of the same lithology (i.e., rocks that may appear similar in the field) may also provide the mechanical contrast required to influence dyke propagation and fault zone architecture. We further note that the pore geometry within lava is also likely to vary within an individual flow unit (e.g., Planke, 1994; Self et al., 1998). Therefore, for example, a difference in Young's modulus between the top of a lava unit that contains spherical pores and the base that contains flattened pores (i.e., pores with their pore major axis parallel to the macroscopic bedding) may be sufficient to hamper dyke propagation.

To conclude, the mechanical anisotropy within individual units and sequences of volcanic rock can be large due to pore geometry alone. Therefore, the orientation of volcanic blocks collected or catalogued in the field, and an accurate description of their pore geometry, should form an important part of volcanic rock reservoir characterisation (e.g., Millett et al., 2015; Chen et al., 2016) and studies that assess the propagation and arrest of dykes (e.g., Gudmundsson, 2006), and the structural stability of (e.g., Voight, 2000; Apuani et al., 2005; Heap et al., 2015c) and permeability anisotropy in (e.g., Lavallée et al., 2013; Gaunt et al., 2014; Heap and Kennedy, 2016; Farquharson et al., 2016a, 2016b) volcanic edifices.

## 5. Conclusions

Our numerical modelling highlights that pore geometry and orientation (with respect to the loading direction) can greatly influence the compressive strength and Young's modulus of porous rock. Our modelled results align with experimental data for porous basalt (Bubeck et al., 2017), but not with data for porous sandstone (Baud et al., 2005; Louis et al., 2009; and new data). We conclude that the modelling presented herein is particularly relevant for extrusive volcanic rocks, but that the alignment of grains (or platy minerals such as clays) may play a more important role in dictating strength anisotropy in porous sandstones than pore geometry and orientation (as suggested in Louis et al., 2009). There are unfortunately too few data to make firm conclusions as to whether our results are relevant for porous limestones. Through comparison with published data, we show that the strength anisotropy that arises as a result of preferentially aligned elliptical pores is of a similar magnitude to that generated by bedding in porous sandstones and foliation in low-porosity metamorphic rocks. Pore geometry and orientation therefore emerges as an important metric for a variety of geophysical and geotechnical applications, and as an important consideration in the development of new micro-mechanical models designed to explore the mechanical behaviour of porous materials.

## Acknowledgements

The authors of this study gratefully acknowledge a Cai Yuanpei Partenariats Hubert Curien (PHC) grant (project number 36605ZB), implemented and funded by the Ministry of Foreign Affairs (MAEDI) and the Ministry of Higher Education and Research (MENESR) in France, and the Ministry of Education and the China Scholarship Council (CSC) in China. L. Griffiths, M. Heap, and P. Baud also acknowledge LABEX grant ANR-11-LABX-0050 G-EAU-THERMIE-PROFONDE; this study therefore benefits from state funding managed by the Agence National de la Recherche (ANR) as part of the "Investissements d'avenir" program. We gratefully acknowledge Thierry Reuschlé and Marie Lenoir for experimental support. T. Xu acknowledges the National Natural Science Foundation of China (grant number 51474051, 41672301), the National Basic Research Program of China (grant number 2013CB227900 and 2014CB047100), and Fundamental Research Funds for the Central Universities of China (grant number N150102002). We are grateful for the constructive comments of Alodie Bubeck, Hasan Karakul, and Toru Takeshita, which helped improve this manuscript. The paper also benefitted from a conversation with Alan George Heap.

## References

- Al-Harathi, A.A., Al-Amri, R.M., Shehata, W.M., 1999. The porosity and engineering properties of vesicular basalt in Saudi Arabia. *Eng. Geol.* 54, 313–320. [http://dx.doi.org/10.1016/S0013-7952\(99\)00050-2](http://dx.doi.org/10.1016/S0013-7952(99)00050-2).
- Andrews, G.D., Branney, M.J., 2011. Emplacement and rheomorphic deformation of a large, lava-like rhyolitic ignimbrite: grey's Landing, southern Idaho. *Geol. Soc.*

- Am. Bull. 123, 725–743.
- Apuani, T., Corazzato, C., Cancelli, A., Tibaldi, A., 2005. Physical and mechanical properties of rock masses at Stromboli: a dataset for volcano instability evaluation. *Bull. Eng. Geol. Environ.* 64 (4), 419–431.
- Arbaret, L., Bystricky, M., Champallier, R., 2007. Microstructures and rheology of hydrous synthetic magmatic suspensions deformed in torsion at high pressure. *J. Geophys. Res. Solid Earth* 112.
- Arzilli, F., Cilona, A., Mancini, L., Tondi, E., 2016. Using synchrotron X-ray microtomography to characterize the pore network of reservoir rocks: a case study on carbonates. *Adv. Water Resour.* 95, 254–263.
- Ashby, M.F., Sammis, C.G., 1990. The damage mechanics of brittle solids in compression. *Pure Appl. Geophys.* 133, 489–521.
- Baud, P., Louis, L., David, C., Rawling, G.C., Wong, T.-f., 2005. Effects of bedding and foliation on mechanical anisotropy, damage evolution and failure mode. *Geol. Soc. Lond. Special Publ.* 245, 223–249.
- Baud, P., Vajdova, V., Wong, T.F., 2006. Shear-enhanced compaction and strain localization: inelastic deformation and constitutive modeling of four porous sandstones. *J. Geophys. Res. Solid Earth* 111 (B12).
- Baud, P., Wong, T., Zhu, W., 2014. Effects of porosity and crack density on the compressive strength of rocks. *Int. J. Rock Mech. Min. Sci.* 67, 202–211. <http://dx.doi.org/10.1016/j.ijrmms.2013.08.031>.
- Baud, P., Rolland, A., Heap, M.J., Xu, T., Nicolé, M., Ferrand, T., Reuschlé, T., Toussaint, R., Conil, N., 2016. Impact of Stylolites on the mechanical strength of limestones. *Tectonophysics* 690, 4–20.
- Benson, P.M., Meredith, P.G., Platzman, E.S., White, R.E., 2005. Pore fabric shape anisotropy in porous sandstones and its relation to elastic wave velocity and permeability anisotropy under hydrostatic pressure. *Int. J. Rock Mech. Min. Sci.* 42 (7), 890–899.
- Bourbié, T., Zinsner, B., 1985. Hydraulic and acoustic properties as a function of porosity in Fontainebleau Sandstone. *J. Geophys. Res. Solid Earth* 90, 11524–11532. <http://dx.doi.org/10.1029/JB090iB13p11524>.
- Bubeck, A., Walker, R.J., Healy, D., Dobbs, M., Holwell, D.A., 2017. Pore geometry as a control on rock strength. *Earth Planet. Sci. Lett.* 457, 38–48.
- Chang, C., Zoback, M.D., Khaksar, A., 2006. Empirical relations between rock strength and physical properties in sedimentary rocks. *J. Pet. Sci. Eng.* 51, 223–237. <http://dx.doi.org/10.1016/j.petrol.2006.01.003>.
- Chen, Z., Liu, W., Zhang, Y., Yan, D., Yang, D., Zha, M., Li, L., 2016. Characterization of the paleocrusts of weathered Carboniferous volcanics from the Junggar Basin, western China: significance as gas reservoirs. *Mar. Pet. Geol.* 77, 216–234.
- Dingwell, D.B., Lavallée, Y., Hess, K.-U., Flaws, A., Marti, J., Nichols, A.R., Gilg, H.A., Schillinger, B., 2016. Eruptive shearing of tube pumice: pure and simple. *Solid Earth* 7, 1383.
- Donath, F.A., 1972. In: Doe, B.R., Smith, D.K. (Eds.), *Effects of Cohesion and Granularity on Deformational Behaviour of Anisotropic Rock*, vol. 135. *Studies in Mineralogy and Precambrian Geology*, Geological Society of America Memoir, pp. 95–128.
- Farquharson, J., Heap, M.J., Varley, N.R., Baud, P., Reuschlé, T., 2015. Permeability and porosity relationships of edifice-forming andesites: a combined field and laboratory study. *J. Volcanol. Geotherm. Res.* 297, 52–68. <http://dx.doi.org/10.1016/j.jvolgeores.2015.03.016>.
- Farquharson, J.L., Heap, M.J., Lavallée, Y., Varley, N.R., Baud, P., 2016a. Evidence for the development of permeability anisotropy in lava domes and volcanic conduits. *J. Volcanol. Geotherm. Res.* 323, 163–185.
- Farquharson, J.L., Heap, M.J., Baud, P., 2016b. Strain-induced permeability increase in volcanic rock. *Geophys. Res. Lett.* 43 <http://dx.doi.org/10.1002/2016GL071540>.
- Gaunt, H.E., Sammonds, P.R., Meredith, P.G., Smith, R., Pallister, J.S., 2014. Pathways for degassing during the lava dome eruption of Mount St. Helens 2004–2008. *Geology* 42 (11), 947–950.
- Gudmundsson, A., 2006. How local stresses control magma-chamber ruptures, dyke injections, and eruptions in composite volcanoes. *Earth Sci. Rev.* 79, 1–31. <http://dx.doi.org/10.1016/j.earscirev.2006.06.006>.
- Heap, M.J., Kennedy, B.M., 2016. Exploring the scale-dependent permeability of fractured andesite. *Earth Planet. Sci. Lett.* 447, 139–150.
- Heap, M.J., Xu, T., Chen, C., 2014. The influence of porosity and vesicle size on the brittle strength of volcanic rocks and magma. *Bull. Volcanol.* 76, 1–15.
- Heap, M.J., Xu, T., Kushnir, A.R.L., Kennedy, B.M., Chen, C., 2015a. Fracture of magma containing overpressurised pores. *J. Volcanol. Geotherm. Res.* 301, 180–190. <http://dx.doi.org/10.1016/j.jvolgeores.2015.05.016>.
- Heap, M.J., Brantut, N., Baud, P., Meredith, P.G., 2015b. Time-dependent compaction band formation in sandstone. *J. Geophys. Res. Solid Earth* 120 (7), 4808–4830.
- Heap, M.J., Farquharson, J.L., Baud, P., Lavallée, Y., Reuschlé, T., 2015c. Fracture and compaction of andesite in a volcanic edifice. *Bull. Volcanol.* 77 (6), 1–19.
- Heap, M.J., Wadsworth, F.B., Xu, T., Chen, C., Tang, C., 2016. The strength of heterogeneous volcanic rocks: a 2D approximation. *J. Volcanol. Geotherm. Res.* 319, 1–11. <http://dx.doi.org/10.1016/j.jvolgeores.2016.03.013>.
- Heap, M.J., Violay, M., Wadsworth, F.B., Vasseur, J., 2017. From rock to magma and back again: the evolution of temperature and deformation mechanism in conduit margin zones. *Earth Planet. Sci. Lett.* 463, 92–100.
- Jaeger, J.C., Cook, N.G., Zimmerman, R., 2009. *Fundamentals of Rock Mechanics*. John Wiley & Sons.
- Ji, Y., Baud, P., Vajdova, V., Wong, T.-f., 2012. Characterization of pore geometry of Indiana limestone in relation to mechanical compaction. *Oil Gas. Sci. Technol. D'IFF Energy Nouv.* 67, 753–775.
- Ji, Y., Hall, S.A., Baud, P., Wong, T.-f., 2015. Characterization of pore structure and strain localization in Majella limestone by X-ray computed tomography and digital image correlation. *Geophys. J. Int.* 200, 701–719.
- Kachanov, M., Tsukrov, I., Shafiro, B., 1994. Effective moduli of solids with cavities of various shapes. *Appl. Mech. Rev.* 47 (1S), 151–174.
- Karakul, H., Ulusay, R., Isik, N.S., 2010. Empirical models and numerical analysis for assessing strength anisotropy based on block punch index and uniaxial compression tests. *Int. J. Rock Mech. Min. Sci.* 47, 657–665.
- Klein, E., Baud, P., Reuschlé, T., Wong, T.F., 2001. Mechanical behaviour and failure mode of Bentheim sandstone under triaxial compression. *Phys. Chem. Earth, Part A Solid Earth Geodesy* 26 (1–2), 21–25.
- Kushnir, A.R., Martel, C., Champallier, R., Arbaret, L., 2017. In situ confirmation of permeability development in shearing bubble-bearing melts and implications for volcanic outgassing. *Earth Planet. Sci. Lett.* 458, 315–326. <http://dx.doi.org/10.1016/j.epsl.2016.10.053>.
- Lavallée, Y., Benson, P.M., Heap, M.J., Hess, K.U., Flaws, A., Schillinger, B., Meredith, P.G., Dingwell, D.B., 2013. Reconstructing magma failure and the degassing network of dome-building eruptions. *Geology* 41 (4), 515–518.
- Lemaître, J., Chaboche, J.-L., 1994. *Mechanics of Solid Materials*. Cambridge University Press.
- Louis, L., David, C., Robion, P., 2003. Comparison of the anisotropic behaviour of undeformed sandstones under dry and saturated conditions. *Tectonophysics* 370 (1), 193–212.
- Louis, L., Baud, P., Wong, T.-f., 2009. Microstructural inhomogeneity and mechanical anisotropy associated with bedding in Rothbach sandstone. *Pure Appl. Geophys.* 166, 1063–1087.
- Luoqot, L., Hebert, V., Rodriguez, O., 2016. Calculating structural and geometrical parameters by laboratory measurements and X-ray microtomography: a comparative study applied to a limestone sample before and after a dissolution experiment. *Solid Earth* 7, 441–456.
- Marti, J., Soriano, C., Dingwell, D.B., 1999. Tube pumices as strain markers of the ductile–brittle transition during magma fragmentation. *Nature* 402, 650–653.
- Millett, J., Hole, M., Jolley, D., Schofield, N., Campbell, E., 2015. Frontier exploration and the north Atlantic igneous province: new insights from a 2.6 km offshore volcanic sequence in the NE Faroe–shetland basin. *J. Geol. Soc.* 173 <http://dx.doi.org/10.1144/0016-76492015-069>.
- Millien, A., 1993. *Comportement anisotrope du grès des Vosges : élasto-plasticité, localisation, rupture*. Thèse de Doctorat en Sciences. Université Joseph Fourier, Grenoble.
- Okumura, S., Nakamura, M., Nakano, T., Uesugi, K., Tsuchiyama, A., 2010. Shear deformation experiments on vesicular rhyolite: implications for brittle fracturing, degassing, and compaction of magmas in volcanic conduits. *J. Geophys. Res. Solid Earth* 115.
- Planke, S., 1994. Geophysical response of flood basalts from analysis of wire line logs: Ocean Drilling Program Site 642, Vøring volcanic margin. *J. Geophys. Res. Solid Earth* 99 (B5), 9279–9296.
- Quane, S.L., Russell, J.K., Friedlander, E.A., 2009. Time scales of compaction in volcanic systems. *Geology* 37 (5), 471–474.
- Rice, R.W., 1997. Limitations of pore-stress concentrations on the mechanical properties of porous materials. *J. Mater. Sci.* 32, 4731–4736. <http://dx.doi.org/10.1023/A:1018674713006>.
- Robion, P., David, C., Dautriat, J., Colombier, J.C., Zinsmeister, L., Collin, P.Y., 2014. Pore fabric geometry inferred from magnetic and acoustic anisotropies in rocks with various mineralogy, permeability and porosity. *Tectonophysics* 629, 109–122.
- Rozenbaum, O., Rolland du Roscat, S., 2014. Representative elementary volume assessment of three-dimensional x-ray microtomography images of heterogeneous materials: Application to limestones. *Phys. Rev. E* 89, 53304. <http://dx.doi.org/10.1103/PhysRevE.89.053304>.
- Sammis, C.G., Ashby, M.F., 1986. The failure of brittle porous solids under compressive stress states. *Acta Metall.* 34, 511–526. [http://dx.doi.org/10.1016/0001-6160\(86\)90087-8](http://dx.doi.org/10.1016/0001-6160(86)90087-8).
- Schaefer, L.N., Kendrick, J.E., Oommen, T., Lavallée, Y., Chigna, G., 2015. Geomechanical rock properties of a basaltic volcano. *Front. Earth Sci.* 3, 29. <http://dx.doi.org/10.3389/feart.2015.00029>.
- Schmitt, M., Halisch, M., Müller, C., Fernandes, C.P., 2016. Classification and quantification of pore shapes in sandstone reservoir rocks with 3-D X-ray micro-computed tomography. *Solid Earth* 7, 285–300.
- Self, S., Kesztelyi, L., Thordarson, T., 1998. The importance of pāhoehoe. *Annu. Rev. Earth Planet. Sci.* 26 (1), 81–110.
- Shea, W.T., Kronenberg, A.K., 1993. Strength and anisotropy of foliated rocks with varied mica contents. *J. Struct. Geol.* 15 (9–10), 1097–1121.
- Shea, T., Houghton, B.F., Gurioli, L., Cashman, K.V., Hammer, J.E., Hobden, B.J., 2010. Textural studies of vesicles in volcanic rocks: an integrated methodology. *J. Volcanol. Geotherm. Res.* 190, 271–289. <http://dx.doi.org/10.1016/j.jvolgeores.2009.12.003>.
- Shields, J.K., Mader, H.M., Pistone, M., Caricchi, L., Floess, D., Putlitz, B., 2014. Strain-induced outgassing of three-phase magmas during simple shear. *J. Geophys. Res. Solid Earth* 119, 6936–6957.
- Simmons, G., Richter, D., 1976. Microcracks in rocks. *Phys. Chem. Min. Rocks* 105–137.
- Tang, C., 1997. Numerical simulation of progressive rock failure and associated seismicity. *Int. J. Rock Mech. Min. Sci.* 34, 249–261.
- Tsukrov, I., Kachanov, M., 1997. Stress concentrations and microfracturing patterns in a brittle-elastic solid with interacting pores of diverse shapes. *Int. J. Solids Struct.* 34, 2887–2904. [http://dx.doi.org/10.1016/S0020-7683\(96\)00202-8](http://dx.doi.org/10.1016/S0020-7683(96)00202-8).
- Vasseur, J., Wadsworth, F.B., Lavallée, Y., Hess, K.U., Dingwell, D.B., 2013. Volcanic

- sintering: timescales of viscous densification and strength recovery. *Geophys. Res. Lett.* 40 (21), 5658–5664.
- Voight, B., 2000. Structural stability of andesite volcanoes and lava domes. *Philos. Trans. R. Soc. Lond. A Math. Phys. Eng. Sci.* 358 (1770), 1663–1703.
- Wadsworth, F.B., Vasseur, J., Scheu, B., Kendrick, J.E., Lavallée, Y., Dingwell, D.B., 2016. Universal scaling of fluid permeability during volcanic welding and sediment diagenesis. *Geology* 44, 219–222.
- Walker, R.J., Holdsworth, R.E., Imber, J., Faulkner, D.R., Armitage, P.J., 2013. Fault zone architecture and fluid flow in interlayered basaltic volcanoclastic–crystalline sequences. *J. Struct. Geol.* 51, 92–104.
- Wang, B., Chen, Y., Wong, T.-f., 2008. A discrete element model for the development of compaction localization in granular rock. *J. Geophys. Res.* 113 <http://dx.doi.org/10.1029/2006JB004501>.
- Weibull, W., 1951. A statistical distribution function of wide applicability. *J. Appl. Mech.* 103, 293–297.
- Wong, T.-f., Wong, R.H.C., Chau, K.T., Tang, C.A., 2006. Microcrack statistics, Weibull distribution and micromechanical modeling of compressive failure in rock. *Mech. Mater.* 38, 664–681. <http://dx.doi.org/10.1016/j.mechmat.2005.12.002>.
- Wright, H.M.N., Roberts, J.J., Cashman, K.V., 2006. Permeability of anisotropic tube pumice: model calculations and measurements. *Geophys. Res. Lett.* 33, L17316. <http://dx.doi.org/10.1029/2006GL027224>.
- Xu, T., Tang, C., Zhao, J., Li, L., Heap, M.J., 2012. Modelling the time-dependent rheological behaviour of heterogeneous brittle rocks. *Geophys. J. Int.* 189, 1781–1796.
- Zambrano, M., Tondi, E., Mancini, L., Arzilli, F., Lanzafame, G., Materazzi, M., Torrieri, S., 2017. 3D Pore-network quantitative analysis in deformed carbonate grindstones. *Mar. Petrol. Geol.* <http://dx.doi.org/10.1016/j.marpetgeo.2017.02.001>.
- Zhu, W., Baud, P., Vinciguerra, S., Wong, T.-f., 2011. Micromechanics of brittle faulting and cataclastic flow in Alban Hills Tuff. *J. Geophys. Res. Solid Earth* 106. <http://dx.doi.org/10.1029/2010JB008046>.
- Zhu, W., Baud, P., Vinciguerra, S., Wong, T.-f., 2016. Micromechanics of brittle faulting and cataclastic flow in Mt Etna basalt. *J. Geophys. Res. Solid Earth* 121. <http://dx.doi.org/10.1002/2016JB012826>.